

PAPER • OPEN ACCESS

Second harmonic generation and ferromagnetic resonance of BaTiO_3 - BiFeO_3 films and nanorod arrays

To cite this article: Nicholas W G Smith *et al* 2025 *J. Phys. Mater.* **8** 035009

View the [article online](#) for updates and enhancements.

You may also like

- [From wide to ultrawide-bandgap semiconductors for high power and high frequency electronic devices](#)
Kelly Woo, Zhengliang Bian, Maliha Noshin *et al.*
- [Near-infrared-detectable artificial synapses for advanced neuromorphic vision applications](#)
Minjun Choi, Gwoncheol Choi, Seungbeom Lee *et al.*
- [2024 roadmap on 2D topological insulators](#)
Bent Weber, Michael S Fuhrer, Xian-Lei Sheng *et al.*

High-purity metals, alloys and polymers

FACILITATING RESEARCH AT THE FOREFRONT OF SCIENTIFIC INNOVATION

Advent Research Materials supplies high-purity metals, alloys and polymers to the global scientific research community.

With an extensive product catalogue, typical purities from 99.0% to 99.999% and multiple forms available, Advent makes it easy to source the materials you require.



ADVENT-RM.COM
INFO@ADVENT-RM.COM
TEL +44 1865 88 4440

ORDER ONLINE OR CONTACT US TO DISCUSS YOUR REQUIREMENTS



PAPER

OPEN ACCESS

RECEIVED
20 February 2025REVISED
18 June 2025ACCEPTED FOR PUBLICATION
2 July 2025PUBLISHED
21 July 2025

Original Content from
this work may be used
under the terms of the
[Creative Commons
Attribution 4.0 licence](#).

Any further distribution
of this work must
maintain attribution to
the author(s) and the title
of the work, journal
citation and DOI.



Second harmonic generation and ferromagnetic resonance of BaTiO₃–BiFeO₃ films and nanorod arrays

Nicholas W G Smith^{1,3}, Rathsara R H H Mudiyansele^{1,3}, Shuang Wu¹, Satoru Emori¹ , Brenden A Magill¹ , Shashank Priya² and Giti A Khodaparast^{1,*}

¹ Department of Physics, Virginia Tech, Blacksburg, VA 24061, United States of America

² Materials Research Institute, Penn State, University Park, PA 16802, United States of America

³ Authors with equal contributions.

* Author to whom any correspondence should be addressed.

E-mail: khoda@vt.edu

Keywords: second harmonic generation, magneto-electric, ferromagnetic resonance, multiferroics, spintronics, nonlinear optics

Abstract

The solid solution of BaTiO₃–BiFeO₃ (BTO–BFO) exhibits enhanced magneto-electric coupling compared to the widely explored BiFeO₃. In this study, we examined BTO–BFO nanorod arrays (and films) ranging from 200 to 600 nm in height (and thickness) by employing second harmonic emission (SHE) and ferromagnetic resonance (FMR) measurements. We demonstrated a large enhancement in SHE in nanorod arrays compared to the films, which can be attributed to the high surface-to-volume ratio in the nanorod arrays. Our FMR measurements showed low effective damping parameters of $(4\text{--}8) \times 10^{-3}$ in both nanorods and film structures. These observations are promising for future nonlinear optoelectronics and spintronics applications.

1. Introduction

Magneto-electric (ME) phenomena in which a magnetic or electric polarization is induced via an external electric or magnetic field have attracted renewed research interest because of the possibility of creating novel electronic and optoelectronic devices. Multifunctional ME materials, with their enhanced coupling between electronic, vibrational, and spin degrees of freedom, are ushering in a new era of revolutionary advances in optoelectronics, spintronics, and quantum information and sensing [1–5]. To harness the full potential of ME phenomena, extensive characterization techniques in conjunction with material design and processing approaches are required.

Bismuth ferrite, BiFeO₃ (BFO), is a well-known type-I single-phase ME in which its multiferroicity comes from two separate mechanisms: Bi 6s lone pairs contribute to ferroelectric ordering, and Fe 3d electrons yield antiferromagnetic ordering. BFO is also one of the very few room temperature MEs, with the potential for very low voltage switching of magnetism [6]. However, BFO demonstrates weak ME coupling with a zero linear ME term due to canceling over its unique spin-spiral structure [7].

Replacement of the Bi and Fe sites through doping, creation of solid solutions, and creation of BFO-based nanorods [8] and nanoparticles [9] can enhance the multiferroic behavior of BFO. A study by Priya's group [10] has reported giant ME coupling in laminate film structures grown on magnetostrictive substrates, opening new avenues for promising new nonlinear effects in nanostructured materials. Investigations on $(1-x)\text{BaTiO}_3-(x)\text{BiFeO}_3$ (BTO–BFO) compositions near the morphotropic phase boundary show the emergence of strong ME coupling. The enhancement of magnetic properties with decreasing BiFeO₃ mole fraction, from 0.775 to 0.750, was attributed to active spin modulation of ordered Fe–O–Fe. It was found that the substitution of large Ba²⁺ and Ti⁴⁺ ions on the A- and B-sites, respectively, enlarges the distortion of the bond angle of Fe–O–Fe to release the spiral magnetic modulation. This material was found to be rhombohedral, on average, with local monoclinic distortions/symmetry, indicating the possibility of polarization enhancement through the presence of intermediate bridging phases [11]. However, there is a lack of optical characterization of the ME-enhanced solid solutions as well as an understanding of the differences between BTO–BFO films and nanostructures.

Due to the lack of inversion symmetry in BFO coupled with its unique ME properties, there has been a growing interest in BFO for nonlinear optical applications. These include applications in actuators, sensors, transducers [12–14], efficient second and third harmonic optical biosensors with magnetic sensitivity, and electro-optical modulators [15, 16]. In our earlier studies, we provided insights on the coherent optical response of our BTO–BFO films and nanorod arrays by generating and detecting coherent phonons, also known as Brillouin oscillations [17]. In this work, we present results to better understand its nonlinear optical properties, and we utilize ferromagnetic resonance (FMR) to observe the magnetic character of our BTO–BFO solid solution in order to better understand the spin dynamics present within our heterostructures. We should note that the presence of magnetic order could lead to further enhancement of nonlinear optical responses due to the decreased symmetry of the envelope functions for electrons, enhancing the second-order nonlinear susceptibility [18–20].

More specifically, in the area of nonlinear optical materials, LiNbO₃ single crystals are currently dominating the electric-optical modulators applications; however, there has been renewed interest in employing other materials such as BaTiO₃ (BTO) [21] or BFO [22, 23]. In this direction, one of the advantages of our heterostructures is that they can be easily grown on commercial silicon wafers to be compatible with existing semiconductor devices.

Furthermore, compared to metallic heterostructures, which experience large spin dissipation caused by electron scattering, magnetic insulators might be expected to possess very low Gilbert damping. However, there are few magnetic insulators with low damping that have been observed with FMR. These insulators include yttrium iron garnet, whose damping parameter is on the order of 10^{-4} , and coherently strained epitaxial spinel ferrites with damping parameters of 3×10^{-3} [24, 25]. A wider selection of low-damping magnetic insulators for spintronic applications is desired; our BTO–BFO heterostructures could offer an interesting avenue for low-loss ME spintronic devices, where progress has been made in manipulating magnons in BFO by employing its ferroelectric polarization [26, 27].

This paper is divided into several sections. In section 2 we introduce the structures of our BTO–BFO films and nanorods; then in section 3 we present second harmonic generation (SHG) measurements, followed by FMR studies in section 4. In this study, we demonstrate that we can design structures based on this solid solution with low effective Gilbert damping as well as detectable SHG at room temperature.

2. Samples characterization

In this section, we present the structural characteristics of our $(1-x)\text{BaTiO}_3-(x)\text{BiFeO}_3$, $x = 0.725$ (BTO–BFO) films and nanorod arrays, with different thicknesses/heights. We report on six samples: 200, 400, and 600 nm nanorod arrays and films of BTO–BFO. All BTO–BFO samples were grown on LSMO seeds deposited on SiO₂ (1 μm)/Si. We have chosen the mole fraction of $x = 0.725$ because the DC measurements indicated the largest piezoelectric and dielectric responses and ME coupling at this composition [11].

The methods for growing our new BTO–BFO films and the nanorod arrays are similar to our earlier studies, reported elsewhere [17, 28, 29], except they were grown on SiO₂ (1 μm)/Si substrates. A schematic of this structure is shown in figures 1(a) and (b). We note that spherical seeds (30 nm in diameter) of La_{0.67}Sr_{0.33}MnO₃ (LSMO) were deposited on the top of the substrates for both the films and the nanorod arrays to reduce strain in the top layers [17, 28].

The microstructure of BTO–BFO nanorods and films were imaged with field emission scanning electron microscopy (SEM). In the SEM images in figures 2(a)–(f), individual nanorods are clearly resolved. With increasing nanorod height, the average nanorod width increases. The gaps between nanorods are reduced considerably in the 600 nm-tall sample, such that a large fraction of the rods come in direct contact with one another. Such nanorod-to-nanorod impaction could affect the FMR dynamics in the 600 nm-tall sample, as we discuss in section 4. We present in figures 3(a)–(c) top-down SEM images of our BTO–BFO films to display the surface morphology. These SEM images suggest an increase in grain size, possibly accompanied by increased surface roughness, with increasing film thickness. Furthermore, our atomic force microscopy (AFM) results in figures 4(a)–(c) indeed confirm the increased root-mean-square roughness with film thickness: 2.5 nm for the 200 nm-thick film, 5.3 nm for the 400 nm-thick film, and 6.3 nm for the 600 nm-thick film. A Bruker Dimension Icon AFM, in tapping mode, was used here to capture the images.

The x-ray diffraction (XRD) patterns of the BTO–BFO films and nanorods indicate that the films and rods exhibit pure perovskite phase, as shown in figure 5. The films display a preferred crystal orientation along the *c*-axis, which is caused by the thermally induced residual strain from the substrate during the deposition process (figure 5(a)). In contrast, no preferred crystal orientation was observed in the nanorods (figure 5(b)). This indicates that each nanorod is free from the substrate-induced residual strain.

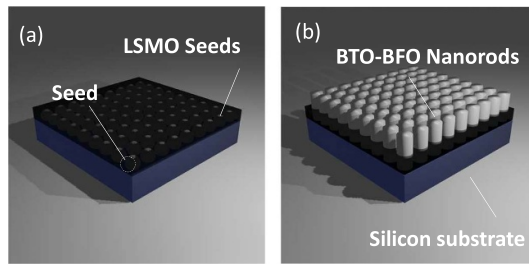


Figure 1. (a) The BTO–BFO structures (nanorods and films) were grown on 30 nm LSMO seeds placed on SiO₂/Si. (b) A schematic of the nanorod arrays grown on the template that is shown in panel (a). The films were grown on a similar template.

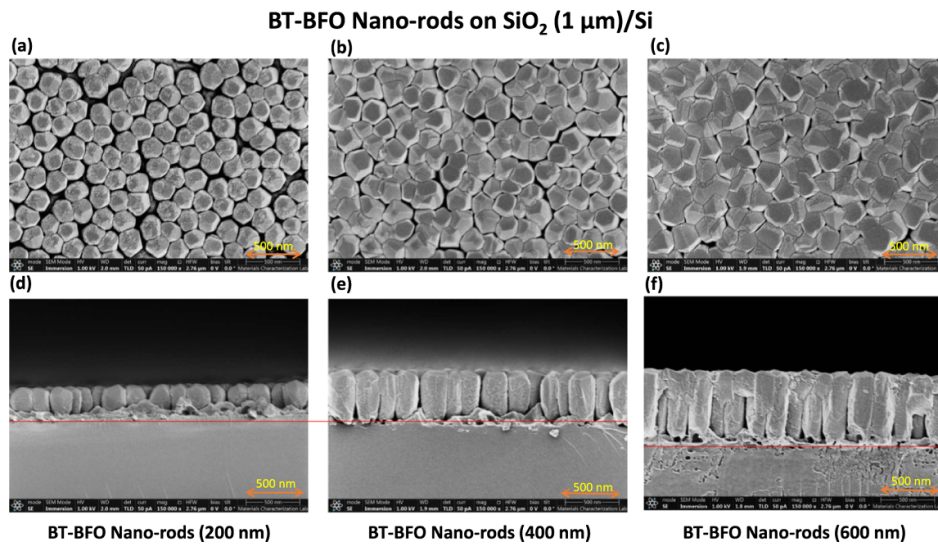


Figure 2. SEM images of BTO–BFO nanorod arrays from (a)–(c) the top–down perspective and (d)–(f) the cross-sectional perspective.

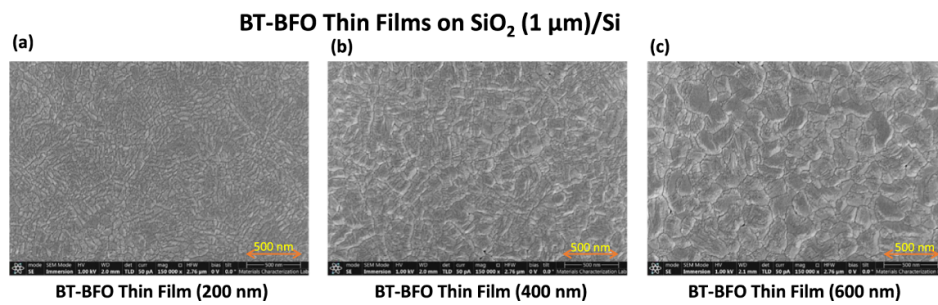


Figure 3. (a)–(c) SEM images of BTO–BFO films from the top–down perspective.

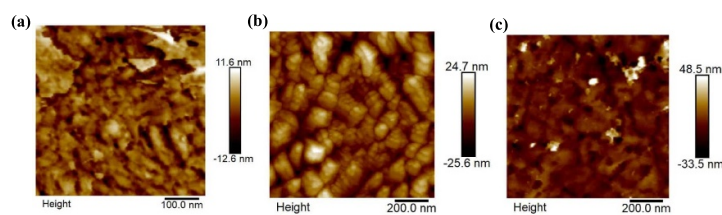
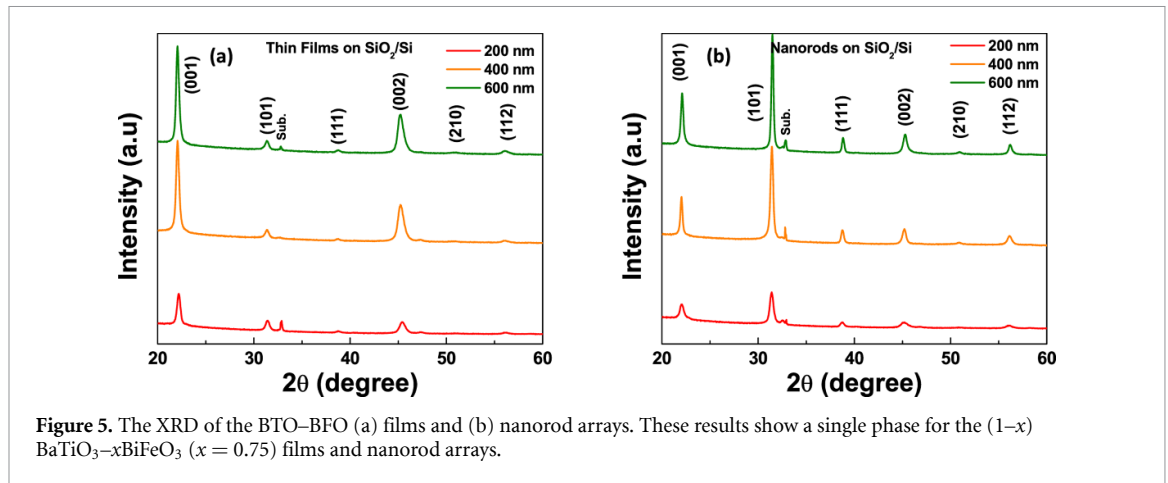


Figure 4. The height plots of our films for (a) 200 nm, (b) 400 nm, and (c) 600 nm films, respectively. The 600 nm film shows a much larger surface roughness.



3. Second harmonic generation in BTO–BFO films and nanorods

It is well known that crystals with magnetic ordering can be centrosymmetric and still exhibit non-zero SHG because the magnetic structure can have lower symmetry than the crystal lattice. Indeed, ‘magnetic’ SHG in magnetically ordered dielectrics has been observed and successfully applied as a useful tool for studying electronic and magnetic properties for both centrosymmetric and non-centrosymmetric materials. The second-order optical nonlinearity is enhanced when magnetic and ferroelectric orderings are strongly coupled. In an extreme case, a single order parameter appears to control both electric and magnetic ordering (*e.g.* MnWO₄), leading to a strong interplay between electric-dipole and magnetic-optical interactions [19, 20, 30–34]. In a magnetically ordered material like BFO, the second-order nonlinear electric susceptibility has both structural and magnetic order parameter contributions: a time-invariant component with a crystallographic contribution and a time-variant component with a linear, spin-dependent contribution. In the case of ferroelectric BTO, the main contribution is from the net dipole moment of the material [35–39].

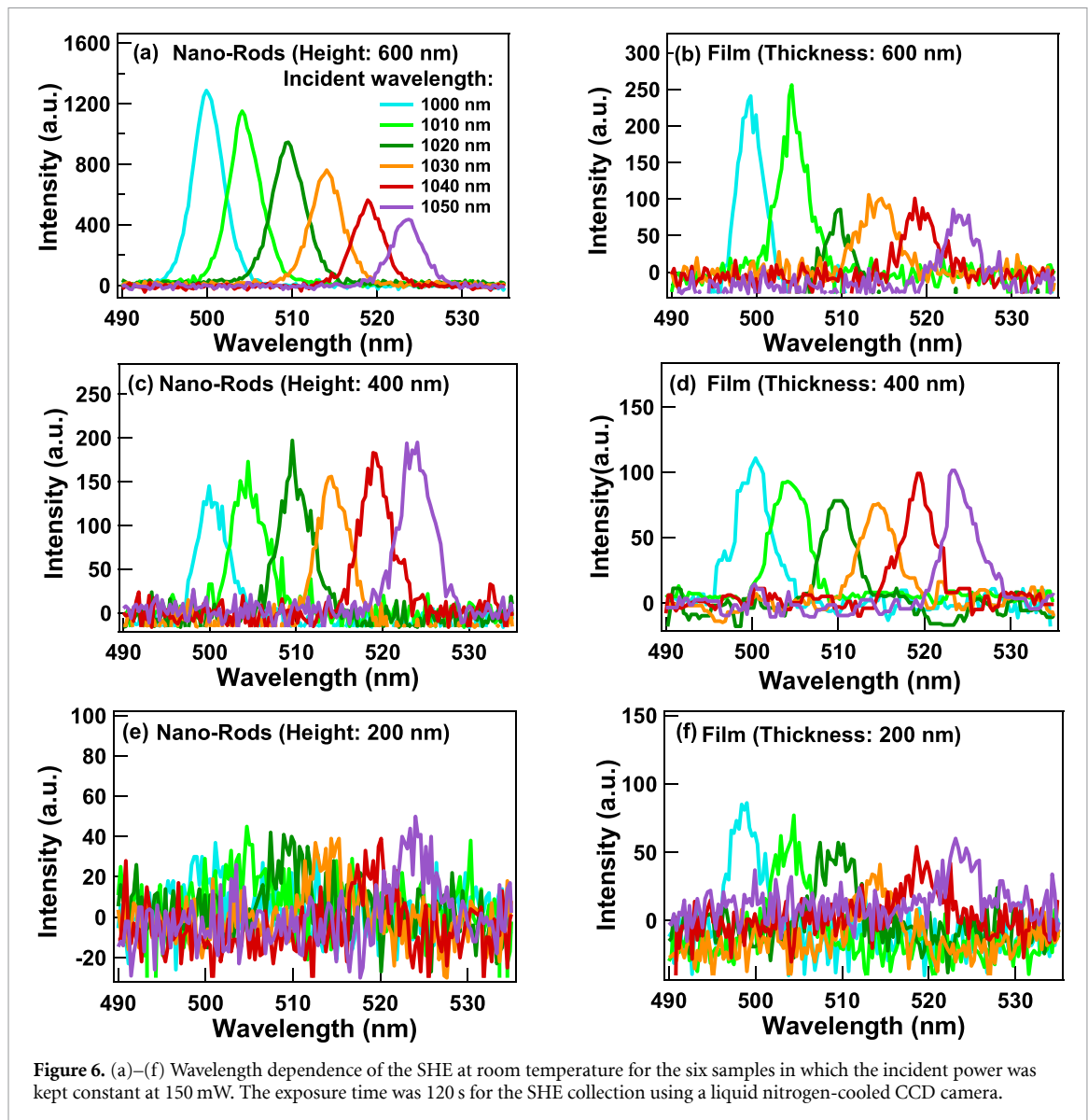
In the present study, we examine nonlinear optical properties of our grown BTO–BFO, where we probed SHG response with excitation wavelengths ranging from 1000–1050 nm. To perform the measurements, we employed a Coherent Chameleon Ti:sapphire oscillator with a repetition rate of 80 MHz and a pulse duration of 100 fs. The second harmonic emissions (SHEs) were measured using a Horiba (iHR550) spectrometer with a liquid nitrogen cooled Symphony II CCD detector, where we kept a 0.15 mm slit size on the spectrometer and a 120 s exposure time to collect the SHE, at room temperature with 150 mW incident laser power.

Figure 6 displays the SHE from our samples at several excitation wavelengths. As shown in this figure, we observed a clear enhancement in SHE amplitudes in our nanorod arrays compared to the films. Our results are in agreement with previous studies that suggest a considerable enhancement of SHE in one dimensional structures compared to films and bulk structures [40–42]. Compared to the films, there is a high surface-to-volume ratio in our nanorod structures. Therefore, even though multiple mechanisms can be responsible for the enhancement of SHG, our observations can be attributed to the high surface-to-volume ratio in the nanorod arrays, which enhances the effective surface dipole contribution, resulting in non-vanishing elements of the nonlinear susceptibility tensor. In particular, as the nanorods are oriented perpendicular to the substrate surface, we expect a large effective surface dipole moment in the radial direction. By employing the approach by Larciprete and Centini [40] and using our SEM images, we identified the normalized surface ratio to be 10, 18, 26 for our 200 nm, 400 nm, and 600 nm nanorod arrays, respectively. We estimated the average rod diameters to be ~ 100 nm.

3.1. Nanorods height and film thickness dependence of SHG

For the nanorod arrays, as shown in figure 6, a continuous decrease in the SHE intensity is observed with the decrease in the nanorods’ height. Nonlinear optical properties of nanorod arrays are strongly influenced by their length-to-diameter ratio (aspect ratio) and surface-to-volume ratio. Thus, our observations can be attributed to the decrease in the surface dipole contribution to the SHE amplitude as the rods’ heights decrease.

Presented in figure 6, we observed a reduction in SHE as the film thickness decreased. If we consider the SHE measured for the film samples at wavelengths of 500 and 505 nm, the intensity of SHE is the highest for the 600 nm thick film and the lowest for the 200 nm thick film. In a polycrystalline film, apart from the bulk contribution to the SHE, part of the SHE can be generated at the grain boundaries or by defects at the grain



boundaries. Furthermore, structural imperfections can break the inversion symmetry, modifying the effective nonlinear optical response. Most studies suggest thickness is not a distinctive factor affecting SHE efficiency [43].

Although there is no hard evidence for a direct correlation between film thickness or crystallite properties of a material with large SHE efficiency, most studies suggest that the enhancement of the SHE can be observed with the reduction of both grain size and crystallinity. In a study by Neumann *et al* [43], several ZnO films were investigated to study the correlation of SHE efficiency with respect to the film thickness and the crystal structure. In their experimental results, the authors were unable to find a clear dependence on thickness or a correlation with the crystallite size. Therefore, they considered another parameter: the normalized surface ratio, which depends on the height and the cross-section of a crystallite by treating them as columns. Their experimental evidence did not show a linear relationship between the SHE efficiency and normalized surface ratio, and an efficient SHE was only observed for a particular range of normalized surface ratio.

3.2. Wavelength dependence of SHG

Figure 7 shows the peak intensity variation as a function of the wavelength for the nanorod arrays (figure 7(a)) and for the films (figure 7(b)). For the 600 nm-tall nanorod sample, we observe a gradual increase in the SHE intensity with the decrease in the incident wavelength. The maximum SHE intensity was detected at a wavelength of 500 nm (with 1000 nm incident light), and the lowest was detected at 525 nm (with 1050 nm incident light). A similar pattern was observed in the films. Different intensities of the observed SHG peak may occur due to a variety of reasons. Here we can consider two main reasons: (1)

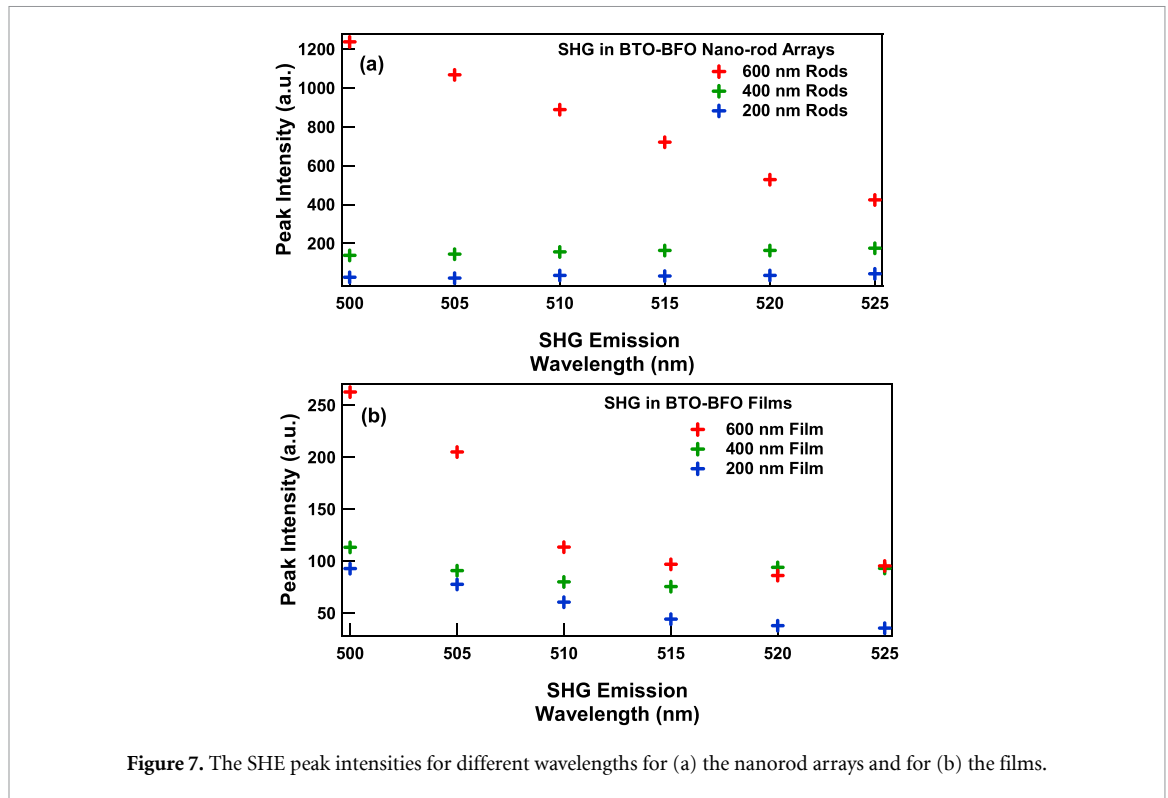


Figure 7. The SHE peak intensities for different wavelengths for (a) the nanorod arrays and for (b) the films.

properties of the incident light such as the incident intensity and frequency, and (2) properties of the material such as nonlinear coefficients which are directly related to the point group symmetry of the material, refractive index profile, and coherence length [44]. The SHE intensity is proportional to the square (I_w^2) of the intensity of the incident beam, considering the incident beam transmits through the material without attenuation. In this study, we maintained a constant incident intensity while changing the incident wavelength.

Another requirement for efficient SHG conversion is satisfying the phase matching condition, *i.e.* the conservation of momentum in the SHG process ($n_\omega = n_{2\omega}$; where n_ω and $n_{2\omega}$ are refractive indices of the fundamental and SHE, respectively). This condition can only be satisfied in a birefringent material. In general, there exists a refractive index dispersion in materials that results in phase mismatch, lowering the SHG efficiency. Furthermore, the competition between different nonlinear optical processes and the energy exchange depend on the wavelength and the intensity of the fundamental laser excitation.

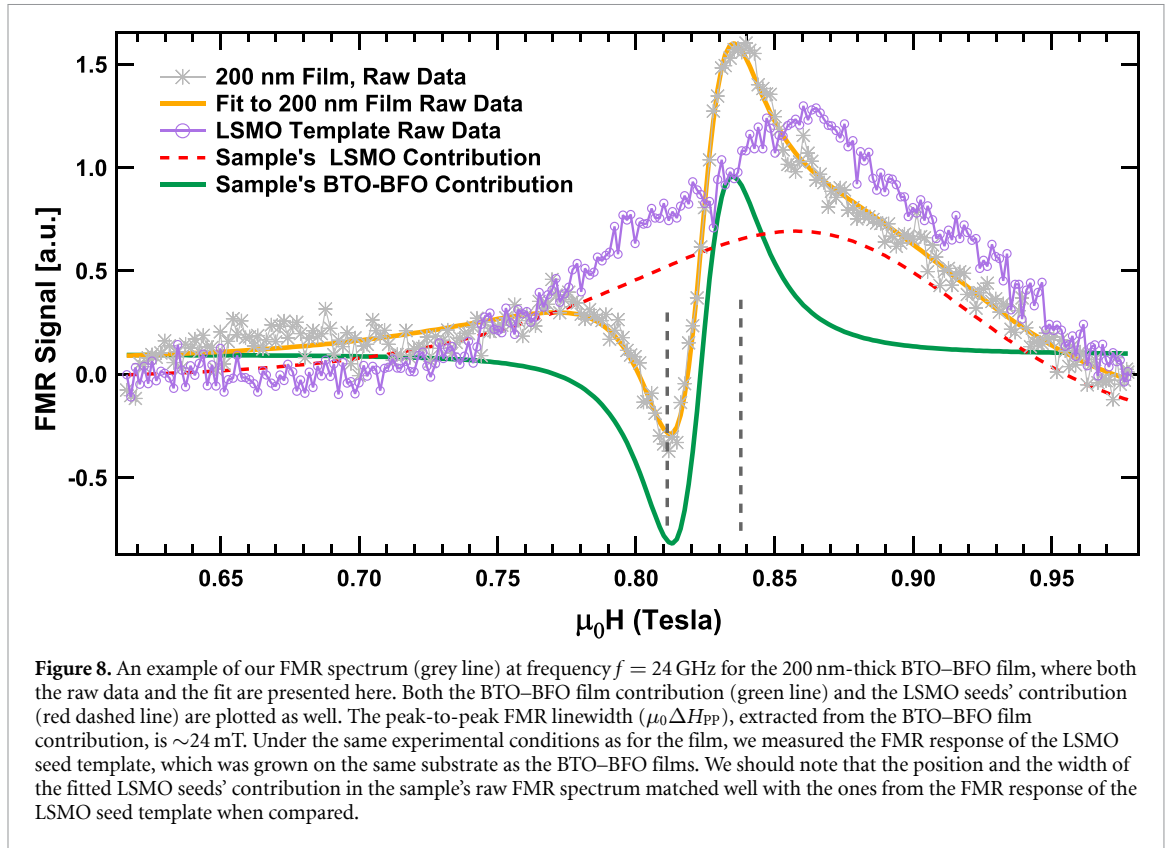
Prasanth *et al* [45] reported SHG and two-photon absorption in a single isolated ZnO nano-wire and identified that SHE could be enhanced when the incident light was tuned near the exciton wavelength. Furthermore, a large enhancement of SHE in our longer BTO–BFO nanorods (with strong wavelength dependence) could be due to the linear Mie scattering enhancement of SHG, which has been previously reported in BTO individual nanoparticles. The Mie resonance is sensitive to the incident wavelength due to the size and distribution of the nanoparticles [46]. In addition, the same group reported the SHE enhancement and wavelength dependence in BTO meta-structures [47].

Aiming for more tunability, miniaturization, and integration on chips, beyond commonly used materials such as LiNbO₃ and BBO, our observations provide the feasibility of employing BTO–BFO films and nanorod arrays, grown on Si, toward SHG applications.

4. FMR

To examine magnetization dynamics in BTO–BFO nanorods and films, we performed broadband FMR spectroscopy. The BTO–BFO samples measured here were grown on LSMO seeds [28] on SiO₂(1 μm)/Si substrates. The sample structure here is distinct from BTO–BFO on epitaxial LSMO on (110)- and (100)-oriented SrTiO₃ characterized by FMR in a previous study [48].

For each FMR measurement, the sample was excited with a fixed microwave frequency from a coplanar waveguide, while a quasi-static magnetic field was applied in the sample plane. By employing a 700 Hz modulation field colinear with the quasi-static field, the resonance signal was acquired with a lock-in



amplifier connected to a microwave diode. Hence, the measured resonance spectrum was the derivative of the microwave absorption with respect to the quasi-static field, as shown in figure 8 for the 200 nm-thick film.

In each of our FMR spectra, we observed a shoulder to the right of the FMR response. This shoulder is attributed to the contribution from the LSMO seeds. In order to confirm this attribution, we measured a template that only included the LSMO seeds. The result is shown in figure 8, where we can see a good match between the fitted LSMO contribution in the BTO-BFO film and the LSMO-only template spectrum. The peak-to-peak FMR linewidth ΔH_{PP} was quantified by fitting the spectrum with a Lorentzian derivative (details shown in an earlier study by Smith *et al*) [49].

We measured the frequency f dependence of $\mu_0\Delta H_{PP}$, as summarized in figures 9(a) and (b). The observed f dependence appears to be approximately linear in all cases. Therefore, we estimate the effective damping parameter α_{eff} with [50]:

$$\mu_0\Delta H_{PP} = \mu_0\Delta H_0 + \left(\frac{2}{\sqrt{3}}\right) \left(\frac{2\pi}{\gamma}\right) \alpha_{\text{eff}} f \quad (1)$$

where μ_0 is the permeability of free space, ΔH_0 is the zero-frequency linewidth (typically attributed to inhomogeneous linewidth broadening), and $\gamma/2\pi = 28$ GHz/T is the gyromagnetic ratio, derived from the f dependence of the resonance field (through a protocol similar to an earlier study by Emori *et al* [24]). As summarized in table 1, the values of α_{eff} for the BTO-BFO nanorods and films are in the range of $(4-8) \times 10^{-3}$. The lower end of this range, *i.e.* obtained for the 200- and 400 nm-tall BTO-BFO nanorods, is comparable to α_{eff} for low-damping insulating ferrite films reported previously [24]. Based on the rather low values of α_{eff} , it might be concluded that these BTO-BFO systems are promising for low-loss ME spintronics.

However, we must point out caveats to the above conclusion. First, we observe large FMR linewidths of $\mu_0\Delta H_{PP} > 10$ mT. These linewidths are an order of magnitude greater than those reported for low-loss insulating ferrite films (*e.g.* $\mu_0\Delta H_{PP} \sim 1$ mT) [24, 25, 51]. A possible source of the large linewidths in the BTO-BFO samples is magnetic inhomogeneity—*i.e.* a broader FMR spectrum arises from a wide distribution of regions with different resonance conditions. The simple linear fit with equation (1) assumes that such inhomogeneous broadening is captured by the zero-frequency linewidth $\mu_0\Delta H_0$. The large values of $\mu_0\Delta H_{PP} > 10$ mT suggest substantial inhomogeneity in the BTO-BFO samples.

Second, the 'effective' damping parameters α_{eff} , obtained from the simple analysis with equation (1), may not accurately quantify the intrinsic Gilbert damping of the BTO-BFO. Specifically, the values of α_{eff} here may include extrinsic non-Gilbert relaxation [49, 50], – such as two-magnon scattering, where the uniform

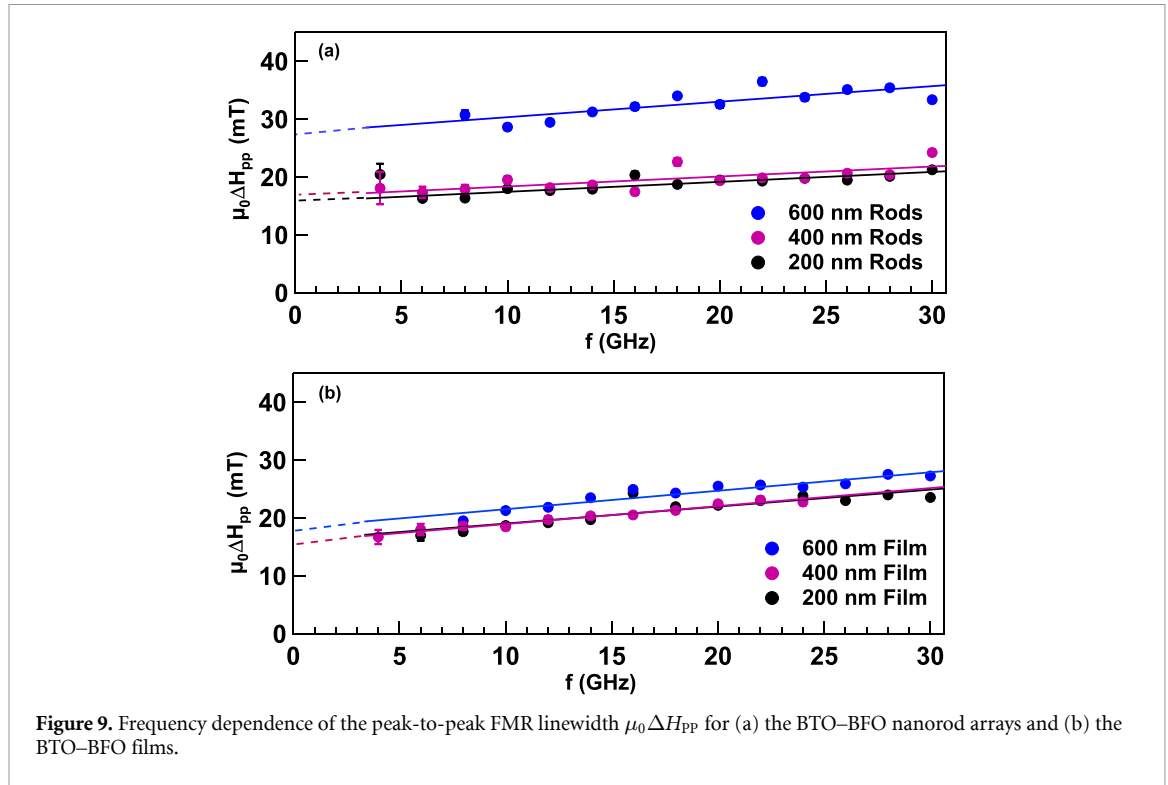


Table 1. Summary of the extracted effective damping parameters and the associated zero-frequency linewidths for the samples studied here.

Sample	$\alpha_{\text{eff}}[10^{-3}]$	$\mu_0\Delta H_0$ [mT]
200 nm nanorods	4.2 ± 0.5	15 ± 1
400 nm nanorods	4.0 ± 1.0	16 ± 1
600 nm nanorods	7.0 ± 2.0	28 ± 1
200 nm film	6.3 ± 0.9	17 ± 1
400 nm film	7.6 ± 0.5	16 ± 1
600 nm film	7.5 ± 0.8	19 ± 1

FMR precessional mode ($k = 0$) decays into a degenerate spin-wave mode ($k \neq 0$) [52]. Two-magnon scattering can be induced by defects in the translational symmetry of the crystalline samples—for instance, the gaps or interfaces between the individual BTO–BFO nanorods and the grain boundaries in the BTO–BFO films. We remark that while two-magnon scattering often manifests as a nonlinear trend in FMR linewidth vs frequency [52], the nonlinearity may be obscured by the limited frequency range and the scatter in our data. The seemingly linear trends in figures 9(a) and (b) do not rule out significant two-magnon scattering.

Still, it is instructive to compare the FMR results of the BTO–BFO samples as summarized in figure 9 and table 1. The most striking finding is that the 600 nm-tall nanorod sample exhibits about 50% greater FMR linewidths than the 200- and 400 nm counterparts. To understand the possible origin of the greater linewidths in the tall nanorod sample, we refer back to the SEM results in figure 2: the nanorods in the 600 nm-tall sample are in direct contact with each other, in contrast to the 200- and 400 nm samples in which the nanorods are well separated.

We speculate that the direct rod-to-rod interfaces between the 600 nm-tall nanorods may lead to substantial localized strain (distinct from the minimal substrate-induced residual strain within the nanorod bulk). Such localized strain modifies the magnetic properties near the interfaces through magnetoelastic coupling, which is known to be strong in BTO–BFO [11]. The effect of this contact strain between 600 nm rods can be seen in the XRD data in figure 5(b) where the (001) and (002) peaks for the 200 and 400 nm rods line up while we observed a shift in the peak's position of the 600 nm rods that is indicative of the longest rods being under additional strain compared to the shorter rods. We should note that in the films (figure 5(a)) the peak position shifted slightly to a lower 2θ by increasing the thickness, an indication of a small tensile strain. As the film thickness increases, we expect a lower strain, induced by the interface with the LSMO seed layer.

The 600 nm-tall sample should then have greater magnetic inhomogeneity, leading to greater inhomogeneous linewidth broadening ΔH_0 . The magnetic inhomogeneity could also enhance two-magnon

scattering, perhaps responsible for the larger α_{eff} for the 600 nm-tall sample compared to the shorter nanorod samples.

Strain-induced magnetic inhomogeneity could also explain the greater FMR linewidths and effective damping for the BTO–BFO films, compared to the 200- and 400 nm nanorod samples. The well-separated 200- and 400 nm nanorods, each grown vertically from a nanoscopic LSMO seed, are likely subjected to less strain, hence stabilizing more homogeneous magnetism and lower ΔH_0 and α_{eff} . In contrast, the growth of a film is constrained by the substrate, leading to non-negligible, non-uniform residual strain. The non-uniform residual strain can yield magnetic inhomogeneity that increases ΔH_0 and α_{eff} in the films.

The FMR linewidths and effective damping are similar among the three BTO–BFO films with different thicknesses, even though the surface roughness varies by more than a factor of two (see figures 4(a)–(c)). Indeed, it is reasonable that the surface should have little effect on the magnetization dynamics of films that are hundreds of nm thick. We speculate that the residual strain is similar within the bulk of these rather thick films, thereby yielding similar ΔH_0 and α_{eff} for all thicknesses.

We emphasize that all BTO–BFO systems studied here have large linewidths exceeding 10 mT. This is the case even for the 200- and 400 nm nanorod samples with ‘low effective damping,’ potentially because different nanorods in the array have slightly different magnetic properties, e.g. due to various crystal orientations. From a practical standpoint, it may be difficult to suppress inhomogeneous broadening or two-magnon scattering in BTO–BFO systems, especially those with macroscopic lateral dimensions spanning numerous nanorods or grains. A better understanding and control of the BTO–BFO crystal growth mechanisms could help attain more monodisperse nanorods and grains. Alternatively, decreasing the lateral dimensions to the μm or sub- μm scale—so that the system consists of only a single isolated nanorod or grain—could potentially reduce inhomogeneous broadening and two-magnon scattering. Thus, although we find large FMR linewidths in the BTO–BFO samples examined here, further engineering could enable low-loss spin dynamics in BTO–BFO systems.

5. Conclusion

We have presented new nonlinear optical responses of the less optically studied BTO–BFO solid solutions. BTO–BFO nanorods demonstrated a large enhancement in SHE efficiency as compared to films due to the large surface-to-volume ratio contributing to radial dipole moments, as well as potential enhancement due to Mie scattering. The nanorods have also demonstrated significant wavelength tunability of SHE efficiency.

We have also demonstrated sizeable and clear FMR signals of our BTO–BFO films and nanorod arrays. We have observed low effective damping parameters on the order of 10^{-3} in all BTO–BFO systems measured here, comparable to moderately low-damping ferrite films. However, the large FMR linewidths of these BTO–BFO systems suggest significant detrimental contributions from inhomogeneities. Further advances in reducing structural and magnetic inhomogeneities, or miniaturization to the single-nanorod or single-grain scale, could make BTO–BFO systems viable platforms for low-loss ME spintronic applications.

Data availability statement

The data cannot be made publicly available upon publication because the cost of preparing, depositing and hosting the data would be prohibitive within the terms of this research project. The data that support the findings of this study are available upon reasonable request from the authors.

Acknowledgments

This material is based upon work supported by the Air Force Office of Scientific Research under award Numbers FA9550-17-1-0341, DURIP funding (FA9550-16-1-0358), and FA9550-24-1-0059. G A K acknowledges the support from the L C Hassinger Fellowship. Dr Min Gyu Kang, who was involved in this project passed away before this submission.

References

- [1] Geng L D, Yan Y, Priya S and Wang Y U 2020 *Phys. Rev. B* **101** 054422
- [2] Sriramdas R, Kang M, Meng M, Kiani M, Ryu J, Sanghadasa M and Priya S 2020 *Adv. Energy Mater.* **10** 1903689
- [3] Geng L D, Yan Y, Priya S and Wang Y U 2019 *Acta Mater.* **166** 493
- [4] Palneedi H *et al* 2018 *ACS Appl. Mater. Interfaces* **10** 11018
- [5] Annapureddy V *et al* 2018 *Energy Environ. Sci.* **11** 818
- [6] Manipatruni S, Nikonov D E, Lin C C, Gosavi T A, Liu H, Prasad B, Huang Y L, Bonturim E, Ramesh R and Young I A 2019 *Nature* **565** 35

- [7] Catalan G and Scott J F 2009 *Adv. Mater.* **21** 2463
- [8] Park T-J, Papaefthymiou G C, Viescas A J, Lee Y, Zhou H and Wong S S 2010 *Phys. Rev. B* **82** 024431
- [9] Park T J, Papaefthymiou G C, Viescas A J, Moodenbaugh A R and Wong S S 2007 *Nano Lett.* **7** 766
- [10] Park C S, Khachatryan A and Priya S 2012 *Appl. Phys. Lett.* **100** 192904
- [11] Yang S C, Kumar A, Petkov V and Priya S 2013 *J. Appl. Phys.* **113** 144101
- [12] Meng K, Li W, Tang X G, Liu Q X and Jiang Y P 2022 *ACS Appl. Electron. Mater.* **4** 2109
- [13] DrDomenico M and Wemple S H 1969 *J. Appl. Phys.* **40** 720
- [14] Otto T, Grafström S, Chaib H and Eng L M 2004 *Appl. Phys. Lett.* **84** 1168
- [15] Schwung S et al 2014 *J. Appl. Phys.* **116** 114306
- [16] Ramos-Gomes F, Möbius W, Bonacina L, Alves F and Markus M A 2019 *Small* **15** 1803776
- [17] Mudiyansele R R H H et al 2019 *J. Mater. Chem. C* **7** 14212
- [18] Li C 2018 *Nonlinear Optics: Principles and Applications* (Springer)
- [19] Kaminski B et al 2009 *Phys. Rev. Lett.* **103** 057203
- [20] Fiebig M, Pavlov V V and Pisarev R V 2005 *J. Opt. Soc. Am. B* **22** 96
- [21] Wessels B W 2007 *Annu. Rev. Mater. Res.* **37** 659
- [22] Sando D et al 2014 *Phys. Rev. B* **89** 195106
- [23] Nan C W, Bichurin M I, Dong S, Viehland D and Srinivasan G 2008 *J. Appl. Phys.* **103** 031101
- [24] Emori S et al 2017 *Adv. Mater.* **29** 1701130
- [25] Emori S and Li P 2021 *J. Appl. Phys.* **129** 020901
- [26] Parsonnet E et al 2022 *Phys. Rev. Lett.* **129** 087601
- [27] Huang X et al 2024 *Nat. Mater.* **23** 898
- [28] Kang M G, Lee S Y, Maurya D, Christopher Winkler a H C S, Moore R B, Sanghadasa M and Priya S 2017 *Adv. Funct. Mater.* **27** 1701542
- [29] Mudiyansele R R H H et al 2021 *J. Phys. Photon.* **3** 034012
- [30] Corn R M and Higgins D A 1994 *Chem. Rev.* **94** 107
- [31] Pavlov V V, Kalashnikova A M, Pisarev R V, Sängler I a Y D R and Bayer M 2005 *Phys. Rev. Lett.* **94** 157404
- [32] Butet J, Brevet P F and Martin O J F 2015 *ACS Nano* **9** 10545
- [33] Lafrentz M, Brunne D, Kaminski B, Pavlov V V, Rodina A V, Pisarev R V, Yakovlev D R, Bakin A and Bayer M 2013 *Phys. Rev. Lett.* **110** 116402
- [34] Malard L M, Alencar T V, Barboza A P M, Mak K F and de Paula A M 2013 *Phys. Rev. B* **87** 201401
- [35] Trassin M, Luca G D, Manz S and Fiebig M 2015 *Adv. Mater.* **27** 4871
- [36] Lofland S E, McDonald K F, Metting C J, Knoesel E, Murakami M, Aronova M A, Fujino S, Wuttig M and Takeuchi I 2006 *Phys. Rev. B* **73** 092408
- [37] Kim D and Hakand Lim D 2013 *J. Korean Phys. Soc.* **62** 734
- [38] Wang J S, Jin Kui-juan G, Hai-zhong G, Jun-xing Wan Q, He Xu L, Li X L, Xu X L and Yang G Z 2016 *Sci. Rep.* **6** 38268
- [39] Kumar A et al 2008 *Appl. Phys. Lett.* **92** 121915
- [40] Larciprete M C and Centini M 2015 *Appl. Phys. Rev.* **2** 031302
- [41] Dang Y, Zhong C, Zhang G, Ju D, Wang L, Xia S, Xia H and Tao X 2016 *Chem. Mater.* **28** 6968
- [42] Bonacina L, Brevet P F, Finazzi M and Celebrano M 2020 *J. Appl. Phys.* **127** 230901
- [43] Neumann U, Grunwald R, Griebner U, Steinmeyer G and Seeber W 2004 *Appl. Phys. Lett.* **84** 170
- [44] Denev S A, Lummen T T A, Barnes E, Kumar A and Gopalan V 2011 *J. Am. Ceram. Soc.* **94** 2699
- [45] Prasanth R, van Vugt L K, Vanmaekelbergh D A M and Gerritsen H C 2006 *Appl. Phys. Lett.* **88** 181501
- [46] Timpu F, Sergeev A, Hendricks N R and Grange R 2017 *ACS Photonics* **4** 76
- [47] Timpu F, Reig Escalé M, Timofeeva M, Strkalj N, Trassin M, Fiebig M and Grange R 2019 *Adv. Opt. Mater.* **7** 1900936
- [48] Madon B, Kang H B, Kang M G, Maurya D, Magill B A, Alves M J, Wegrowe J E, Drouhin H J, Priya S and Khodaparast G A 2018 *AIP Adv.* **8** 105034
- [49] Smith D A et al 2020 *Phys. Rev. Appl.* **14** 34042
- [50] Mewes C K A and Mewes T 2015 Relaxation in magnetic materials for spintronics *Handbook of Nanomagnetism: Applications and Tools* (Pan Stanford Publishing) pp 71–95
- [51] Singh A V, Khodadadi B, Mohammadi J, Keshavarz S, Mewes T, Negi a R D, Galazka Z, Uecker R and Gupta A 2017 *Adv. Mater.* **29** 1701222
- [52] McMichael R and Krivosik P 2004 *IEEE Trans. Magn.* **40** 2